

# A comparative study on finite element methods for dynamic fracture

Jeong-Hoon Song · Hongwu Wang · Ted Belytschko

Received: 4 December 2006 / Accepted: 12 July 2007 / Published online: 15 August 2007  
© Springer-Verlag 2007

**Abstract** The performance of finite element methods for dynamic crack propagation in brittle materials is studied. Three methods are considered: the extended finite element method (XFEM), element deletion method and interelement crack method. The extended finite element method is a method for arbitrary crack propagation without remeshing. In element deletion methods, elements that meet a fracture criterion are deleted. In interelement crack methods, the crack is limited to element edges; the separation of these edges is governed by a cohesive law. We show that XFEM and interelement method show similar crack speeds and crack paths. However, both fail to predict a benchmark experiment without adjustment of the energy release rate. The element deletion method performs very poorly for the refinements studied, and is unable to predict crack branching.

## 1 Introduction

This paper addresses the question: how well can we predict dynamic fracture with current methods. We will see that the outcome is still quite negative. The prediction of dynamic fracture behavior for the modest range of problems considered here is still somewhat beyond current capabilities. The reasons for this do not lie only in the numerics, but in important gaps in our understanding of dynamic fracture processes and how to model them. In particular, it has become clear through the work of Ravichandar and Knauss [1,2] (see, [3] for a compendium) and Marder and Gross [4] that subscale

processes play a critical role in brittle fracture. These subscale processes are not modeled in any existing methods, so crack speed prediction is still not very accurate. Similarly, the prediction of crack paths also lacks robustness.

Here, we will examine three methods for dynamic crack propagation:

1. the extended finite element method
2. the interelement crack method
3. the element deletion method.

The extended finite element method (XFEM) is a methodology for modeling cracks of arbitrary geometry in a finite element method without remeshing. It originated in Belytschko and Black [5] and Moës et al. [6], and was combined with level sets in Stolarska et al. [7] and Belytschko et al. [8]; all of these applications were for static fracture. The method can be viewed as a partition of unity method [9], but in fact, in the treatment of discontinuities by this method, a partition of unity is never constructed. Instead, a discontinuous function that only spans one element and vanishes at the edges is constructed.

Dynamic crack propagation is an application domain for which XFEM is particularly suitable because the most prevalent method for treating crack growth, remeshing, is very awkward for these problems. In most dynamic crack propagation problems, the crack advances over a large part of the mesh, so that remeshing would need to be performed many times. Remeshing is especially daunting for fragmentation simulations, since such simulations would entail very extensive remeshing. Furthermore, the continuity of the solution is quite important in any numerical model, and even with excellent projection schemes, significant discontinuities can be introduced in the velocities, stresses and displacements by remeshing.

J.-H. Song · H. Wang · T. Belytschko (✉)  
Theoretical and Applied Mechanics, Northwestern University,  
Evanston, IL 60208-3111, USA  
e-mail: tedbelytschko@northwestern.edu

J.-H. Song  
e-mail: j-song2@northwestern.edu

XFEM was first applied to dynamic crack propagation in Belytschko et al. [10]. Subsequently, Song et al. [11] used the Hansbo and Hansbo [12] approach which uses the same basis functions; see Areias and Belytschko [13]. Réthoré et al. [14, 15] improved the stability of the explicit time integration scheme and developed an energy conserving dynamic crack propagation algorithm with XFEM. Remmers et al. [16] have introduced an interesting variant of XFEM where they initiate a crack by injecting discontinuities that span three elements at a time.

In the interelement crack method, the crack is modeled by separation along the element edges. Two approaches are used in the interelement crack method. In the original formulation of Xu and Needleman [17], all elements are separated from the beginning of the simulation. The edges are mechanically joined by cohesive laws. In the Ortiz and Camacho [18] approach, the cohesive zones are injected along edges only when a criterion is met or the element edges are contiguous to a crack tip.

The element deletion method is the one of the simplest methods which can simulate fracture problems within the framework of the conventional FEM without complicated modifications. There is no need to explicitly represent strong discontinuities in displacement fields since fractured elements are generically reflected by a set of elements in which the stress is set to zero.

Dynamic crack propagation is a difficult area in which to benchmark different methods because there are no analytical solutions which can readily be compared to numerical results. Therefore, we will make comparisons to experimental results and examine how well the three methods reproduce various aspects of selected experiments.

## 2 Review of XFEM

The implementation of XFEM used in this study is based on Song et al. [11], which differs in performance from Belytschko et al. [10] only in its omission of partially cracked elements. The key idea in the formulation of this method is that the displacement field incorporates the discontinuity as additional terms in the displacement approximation.

Consider an initial domain  $\Omega_0$  as shown in Fig. 1. The motion is described by  $\mathbf{x} = \Phi(\mathbf{X}, t)$  where  $\mathbf{X}$  and  $\mathbf{x}$  denote material and spatial coordinates, respectively. In the current domain, the image of the initial domain  $\Omega_0$  is denoted by  $\Omega$ . We allow this domain to contain an internal discontinuity  $\Gamma_c$  which is enveloped by a region  $\Omega_c$ . Inside of the region  $\Omega_c$ , we defined two local functions  $f(\mathbf{X})$  and  $g(\mathbf{X}, t)$  where  $f(\mathbf{X})$  and  $g(\mathbf{X}, t)$  are the signed distance functions to describe the crack surface and tip geometry, respectively. The surface  $f(\mathbf{X}) = 0$  corresponds to the crack surface denoted by  $\Gamma_c$  and the function  $g(\mathbf{X}, t)$  is defined so that  $g(\mathbf{X}, t) > 0$  along

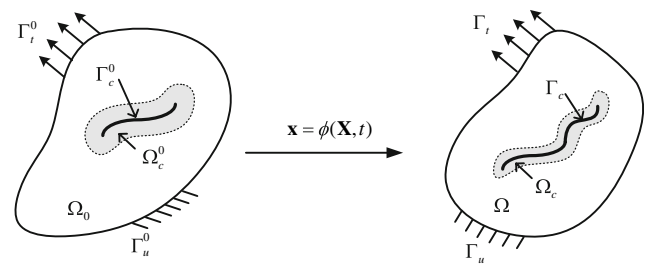


**Fig. 1** A two dimensional body with a discontinuity and its representation in the initial and the current domains

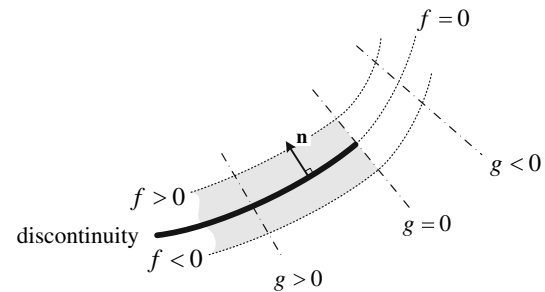


**Fig. 2** A two dimensional discontinuity representation by two implicit functions  $f(\mathbf{X})$  and  $g(\mathbf{X}, t)$

the crack surface and vanishes at the crack tip as shown in Fig. 2. We implicitly define the crack geometry by

$$\mathbf{X}_c^0 \in \Gamma_c^0 \quad \text{if } f(\mathbf{X}) = 0 \quad \text{and} \quad g(\mathbf{X}, t) > 0, \quad \mathbf{X} \in \Omega_c^0 \quad (1)$$

For the numerical representation, we approximate the level set function representation by

$$\sum_I f_I N_I(\mathbf{X}) = 0 \quad (2)$$

where  $f(\mathbf{X}) = \min_{\bar{\mathbf{X}} \in \Gamma_c} \|\mathbf{X} - \bar{\mathbf{X}}\|$ . As a consequence of Eq. (2), the surface of discontinuity can be represented by  $f(\mathbf{X}_I)$  at the nodes of the cracked elements. Then the conventional XFEM displacement field approximation is given by

$$\mathbf{u}^h(\mathbf{X}, t) = \sum_I N_I(\mathbf{X}) \{ \mathbf{u}_I(t) + H(f(\mathbf{X})) H(g(\mathbf{X}, t)) \mathbf{q}_I \} \quad (3)$$

where  $N_I(\mathbf{X})$  is a conventional finite element shape function and  $\mathbf{u}_I$  and  $\mathbf{q}_I$  are the regular and enriched nodal variables, respectively. In XFEM, the enrichment is injected when a criterion for crack nucleation or crack growth is met. In the solutions reported here, we used the loss of material stability criterion (i.e. loss of hyperbolicity), as in [10, 11].

In the calculations reported here, we used the continuum damage model proposed by Lemaitre [19]. The damage evolution law is given by

$$D(\bar{\epsilon}) = 1 - (1 - A)\epsilon_0 \bar{\epsilon}^{-1} - A e^{-B(\bar{\epsilon} - \epsilon_0)} \quad (4)$$

where  $D$  is the damage parameter which can have a value of 0 to 1,  $\bar{\epsilon}$  is the effective strain,  $A$  and  $B$  are material parameters,

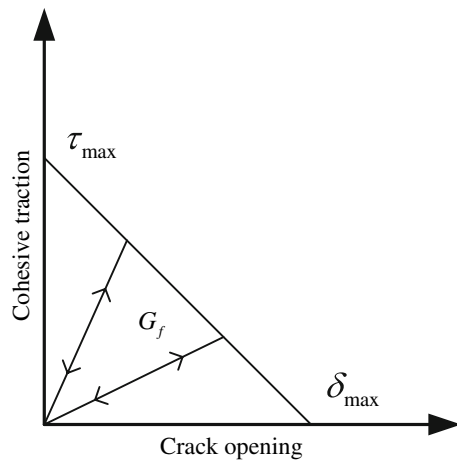


**Fig. 3** Schematic showing of a linear cohesive law: the area under curve is the fracture energy,  $G_f$  of the material

$\epsilon_0$  is the strain threshold, and  $\langle \cdot \rangle$  is the MacCaulay bracket. The constitutive relation is given by

$$\sigma_{ij} = (1 - D)C_{ijkl}\epsilon_{kl} \quad (5)$$

where  $C_{ijkl}$  is the elastic modulus of the undamaged material, and  $\sigma_{ij}$  and  $\epsilon_{kl}$  are stress and strain components, respectively.

### 2.1 Cohesive law

A linear cohesive crack model is used for the modeling of crack surface traction. In this work, we considered only the normal component of the cohesive traction and constructed the cohesive model so that the dissipated energy due to the crack propagation matches the fracture energy, so

$$G_f = \frac{1}{2}\tau_{\max}\delta_{\max} \quad (6)$$

where  $G_f$  is the fracture energy and  $\delta_{\max}$  is the maximum crack opening displacement. The cohesive traction is determined by the cohesive law which relates the traction to the displacement jump across the tip; the cohesive law is also called the traction–separation law for this reason. A traction is applied onto the crack tip surface.

## 3 Review of the element deletion method

The element deletion method is one of the simplest methods for fracture simulation within the framework of the conventional FEM. There is no need to explicitly represent strong discontinuities in displacement fields since fracture is modeled by a set of deleted elements. While the method is called an element deletion method, the element is not deleted, but instead the stress in the element is set to zero. Some programs, such as LS-DYNA [20], remove the mass of the ele-

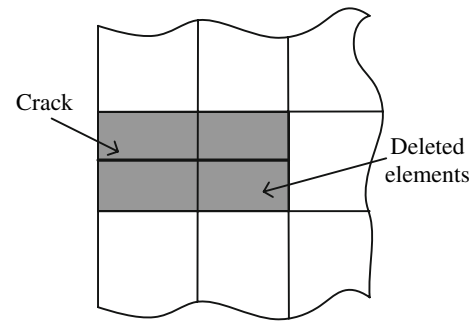


**Fig. 4** Representation of a crack by deleting elements

ment from the global mass matrix to eliminate the inertia effects for these elements, but this seems unwarranted, since the mass does not disappear. We have retained the mass, but for the problems considered here, it makes little difference.

In the element deletion method, the crack is modeled by a set of deleted elements as shown in Fig. 4. More precisely, in these so-called deleted elements, the elements have zero stress, i.e. zero material resistance. This is implemented by using constitutive equations in which the stress tends to zero for sufficiently large strain; examples of such stress–strain laws are shown in Fig. 5.

One of the crucial points in using the element deletion method is the scaling of the constitutive equation. Unless the constitutive equation is adjusted to reflect element size, the released energy due to deleting an element depends on the element size, which causes spurious mesh dependency. To reduce this spurious mesh dependency, the softening curve slope should be scaled so that fracture energy is independent of the element size.

In this paper, we limited our analysis to a linear elastic–linear softening constitutive model as shown in Fig. 6b, which has the damage evolution law given by

$$D(\epsilon^*) = 1 - \frac{\epsilon_0}{\epsilon_1 - \epsilon_0} \left( \frac{\epsilon_1}{\epsilon^*} - 1 \right) \quad (7)$$

where  $\epsilon^*$  is the effective strain and  $\epsilon_0$  and  $\epsilon_1$  are parameters which define the strain at the peak stress and at the complete softening stage, respectively.

The energy dissipation in an element with this stress–strain law is then equated to the surface energy of a crack passing through the element parallel to the sides by modifying the stress–strain law. This energy consistency renders solutions relatively mesh size independent. Generally, no information about the orientation of the crack surface is included, so it is best to use square or nearly square elements.

To obtain energy equivalence in two dimensional problems for the stress–strain law shown in Fig. 6b, the upper strain limit  $\epsilon_1$  is scaled so that

$$G_f h^e = \frac{1}{2} E \epsilon_0 \epsilon_1 A^e \quad (8)$$

**Fig. 5** Schematic showing of stress–strain curves for a material with damage showing: **a** an elastic softening material and **b** a hardening plasticity material

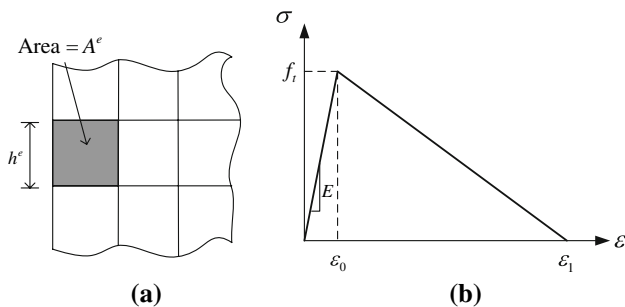
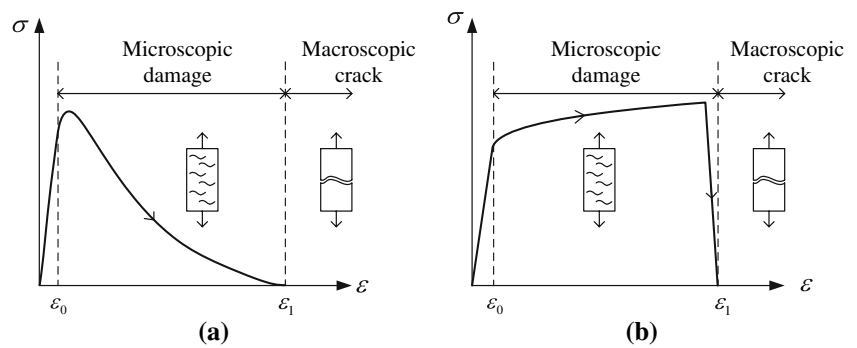


**Fig. 6** Schematic showing of **a** a deleted element and **b** a linear elastic–elastic softening material

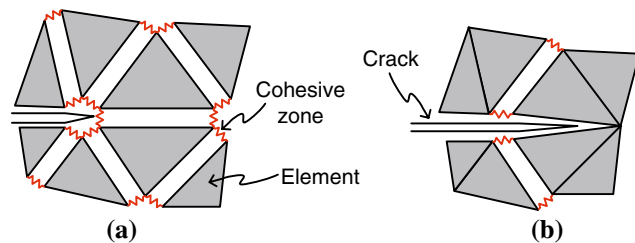


**Fig. 7** Schematic showing of **a** the Xu–Needleman method [17] and **b** the Camacho and Ortiz method [18]

where  $G_f$  is the fracture energy,  $h^e$  is a characteristic dimension (the length of a side for a square element), and  $A^e$  is the area of the element (unit thickness is assumed).

#### 4 The interelement crack method

In the interelement crack method, the crack is modeled by separation along the element edges. This involves adding extra nodes, see Fig. 7. Two approaches are used in the interelement crack method. In the formulation of Xu and Needleman [17], all elements are separated from the beginning of the simulation. The edges are mechanically joined by cohesive

laws of the form

$$\begin{aligned} T_n &= -\frac{\phi_n}{\Delta_n} e^{(-\delta_n/\Delta_n)} \left\{ \frac{\delta_n}{\Delta_n} e^{(-\delta_n^2/\Delta_n^2)} \right. \\ &\quad \left. + \frac{1-q}{r-1} \left[ 1 - e^{(-\delta_n^2/\Delta_n^2)} \right] \left( r - \frac{\delta_n}{\Delta_n} \right) \right\} \\ T_t &= -\frac{\phi_n}{\Delta_n} \left( 2 \frac{\Delta_n}{\Delta_t} \right) \frac{\delta_t}{\Delta_t} \left\{ q + \frac{r-q}{r-1} \frac{\delta_n}{\Delta_n} \right\} e^{(-\delta_n/\Delta_n)} e^{(-\delta_t^2/\Delta_t^2)} \end{aligned} \quad (9)$$

where  $\mathbf{T}$  is the traction across the interelement surface, subscripts  $n$  and  $t$  denote the normal and tangential components, respectively,  $\delta$  is the displacement jump across the cohesive surface interface,  $\phi$  is the cohesive potential function, and  $\Delta$  is a characteristic length; for details, see [17]. In the Ortiz and Camacho [18] approach, elements are allowed to separate along edges only when a criterion is met or the element edges are contiguous to a crack tip: the criterion is given by

$$\sigma^{\text{eff}} = \sqrt{\sigma_n^2 + \beta^{-2} \sigma_t^2} \geq \sigma_{fr} \quad (10)$$

where  $\sigma_n$  and  $\sigma_t$  are the normal and tangential stress along a element edge, respectively.  $\sigma_{fr}$  is the material fracture strength. The cohesive law used in Camacho and Ortiz is

$$\begin{aligned} T_n &= e \frac{\sigma_c}{\delta_c} \beta^2 \delta_s e^{-\delta/\delta_c} \\ T_t &= e \frac{\sigma_c}{\delta_c} \delta_n e^{-\delta/\delta_c} \end{aligned} \quad (11)$$

where  $\sigma_c$  and  $\delta_c$  are the maximum cohesive traction and critical opening displacement, respectively; for details, refer [18]. Once a criterion for insertion of the cohesive law is met, the crack automatically chooses its path by solving the momentum equation that takes into account the traction forces on the cohesive edges. The method is further developed in Ortiz and Pandolfi [21].

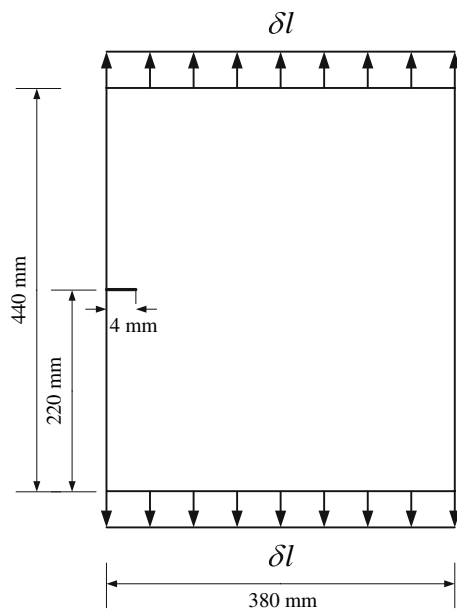


**Fig. 8** Experimental set up for an edge-cracked PMMA plate under displacement control

## 5 Benchmark problems

### 5.1 Comparisons of crack propagation speeds with experiments

Here we examine the quantitative agreement between crack tip propagation speeds for various numerical methods and experimental results [22, 23]. The experiments were conducted in a  $380 \times 440$  mm PMMA plate with an initial notch midway from the left vertical boundary. A schematic showing the experimental setup is shown in Fig. 8; a more detailed description can be found in Fineberg et al. [22]. In the experiment, the specimen is first loaded by displacement control and the applied displacement is very slowly increased every 10–20 s to eliminate elastic waves. Because 10–20 s is too long for explicit dynamic simulations, we prescribed an initial equilibrium stress just below that needed to trigger crack propagation and then perturbed it. The numerical calculations were made with a structured  $190 \times 220$  quadrilateral or cross triangular meshes; the average element size  $h_e = 2$  mm. The former was used for XFEM and the element deletion method and the latter was used for the interelement crack method. The material properties of a PMMA are  $\rho = 1190.0$  kg/m<sup>3</sup>,  $E = 3.240$  GPa and  $\nu = 0.350$ . For the simulations, we used a central difference time integration scheme with a Courant number of 0.1 for all simulations.

Based on the experimental results, Sharon and Fineberg [23] concluded that there are two crack propagation stages. The first stage is below the critical crack speed of about  $0.4v_R$ , where  $v_R$  is the Rayleigh wave speed; for the PMMA

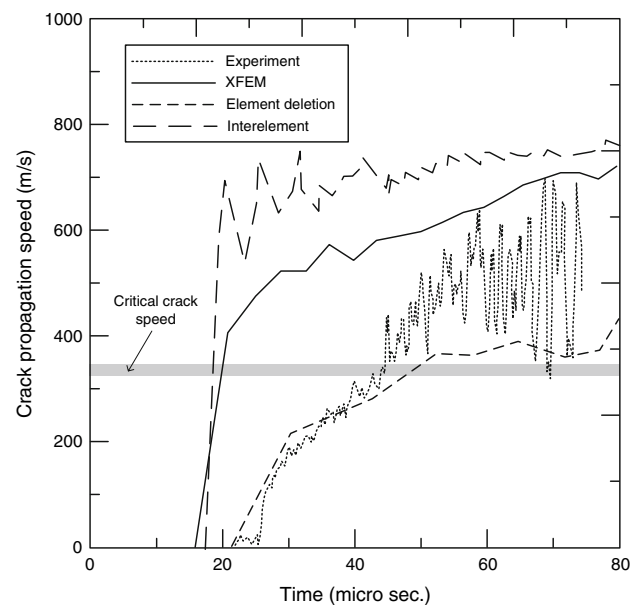


**Fig. 9** Comparison of crack propagation speeds between experiment [23] and various computational methods for fracture energy  $G_f = 500$  Jm<sup>-2</sup>

material, the Rayleigh wave speed is 930 m/s. In this stage, only one main crack is formed and crack speed oscillations rarely occur. In the second stage, after the critical speed is attained, many parasitic micro cracks are formed around the main crack and the crack speed manifests severe oscillations. However the average crack speed seems to reach a stable value around 600 m/s.

Figure 9 shows the computed crack speeds when the fracture energy,  $G_f = 500$  Jm<sup>-2</sup>; this value is in accord with generally reported values of fracture energy of PMMA materials. For the XFEM simulations, the bulk material is a linear elastic and when the maximum tensile strain at the crack tip reached 0.02 strain, we injected a strong discontinuity which is governed by a linear cohesive law: the critical crack opening which corresponds to the fracture energy  $G_f = 500$  Jm<sup>-2</sup> is  $\delta_{\max} = 1.54 \times 10^{-5}$  m. For the element deletion method, we used  $\epsilon_0 = 0.02$ ; note that  $\epsilon_1$  is not a fixed material constant and it can be calculated by Eq. (8) depending on the element size. For the interelement crack method, we used the Camacho and Ortiz cohesive zone model [18] with  $\sigma_c = 75.0$  MPa,  $\delta_c = 2.450 \times 10^{-6}$  m and  $\beta = 1.0$  for Eq. (11). In this case, XFEM and the interelement crack method predict crack speeds substantially above the measured crack speeds. This is due to the fact that the modeling of parasitic micro cracks is missing in XFEM and the resolution is insufficient in the interelement crack method. It is surprising that the crack speed of the interelement crack method is greater than XFEM, since the interelement method generates some parasitic cracks at 45° angles to the main crack, and these should slow the crack. However, the mesh resolution

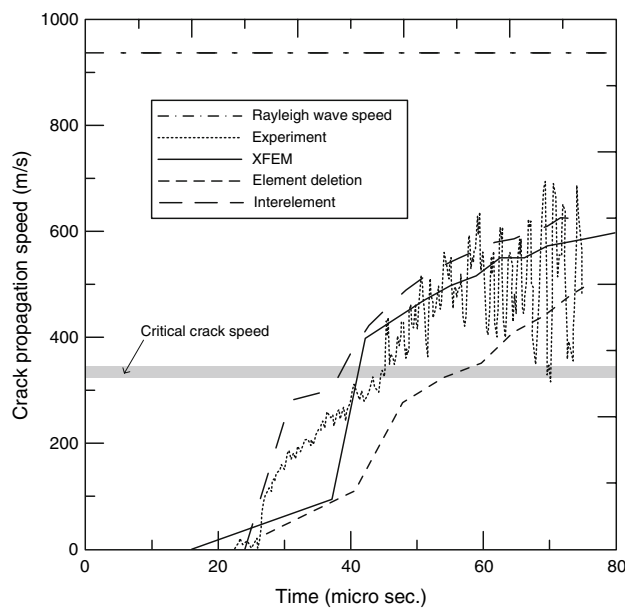
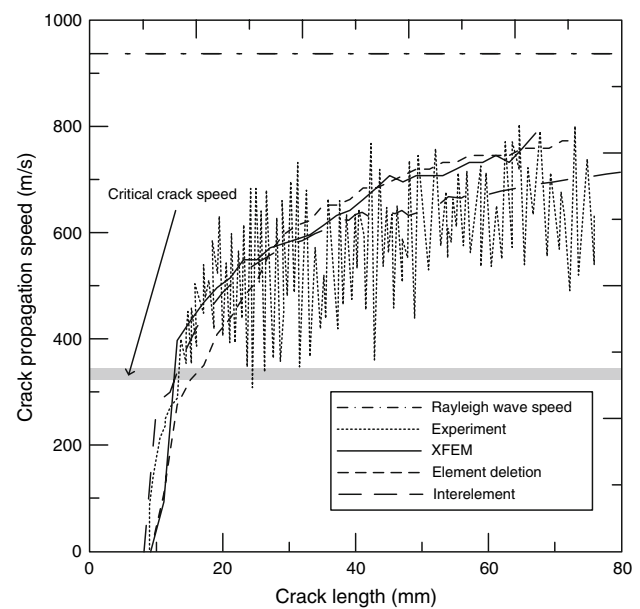


**Fig. 10** Comparison of crack propagation speeds between experiment [23] and various computational methods for  $G_f = 3,000 \text{ Jm}^{-2}$

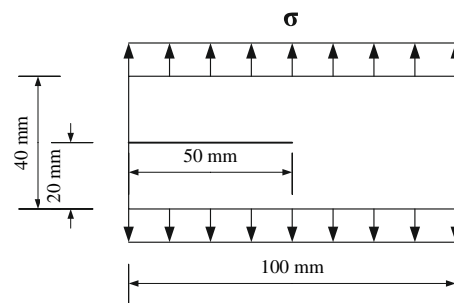
used here is insufficient to mimic the extra energy dissipation associated with the post-critical stage of crack propagation accurately. A discussion of the relation between parasitic cracks and crack propagation speed can be found in Sharon and Fineberg [23].

Figure 10 shows the crack speed as a function of time for  $G_f = 3,000 \text{ Jm}^{-2}$ ; this value was chosen to obtain a better fit to the experimental data [23]. For the XFEM simulations, we used  $\delta_{\max} = 9.260 \times 10^{-5} \text{ m}$  for a linear cohesive law and  $\epsilon_0 = 0.02$  is used for the element deletion method.  $\sigma_c = 75.0 \text{ MPa}$ ,  $\delta_c = 14.715 \times 10^{-6} \text{ m}$  and  $\beta = 1.0$  were used for the interelement crack method. All of the methods predict a crack speed below the Rayleigh wave speed. Before attainment of the critical speed, XFEM and the element deletion method moderately underestimate the crack speed while the interelement crack method overestimates it. However, after the crack propagation speed exceeds the critical speed, both XFEM and the interelement crack method reach a stable value and agree well with the experiment result. Generally, XFEM and interelement crack method give crack propagation speeds near those observed in the experiment, while element deletion underestimates the experimental speed for most of the simulation.

Figure 11 shows the crack speed as a function of crack growth length. Before the crack length reaches 20 mm, XFEM and the interelement crack method match the experiment well while element deletion underestimates the experimental speed. After the crack growth length exceeds 20 mm, the interelement crack method matches the experiment the best while both XFEM and element deletion are somewhat high.



**Fig. 11** Comparison of crack propagation speeds as a function of crack length between experiment [23] and various methods



**Fig. 12** Setup of a dynamic crack branching problem

## 5.2 Dynamic crack branching

The second benchmark problem involves crack growth with branching in a prenotched glass sheet. The material properties are  $\rho = 2,450 \text{ kg/m}^3$ ,  $E = 32 \text{ GPa}$  and  $\nu = 0.20$ . A schematic of the experiment is shown in Fig. 12. As can be seen, a tensile stress  $\sigma_y = 1 \text{ MPa}$  is applied at the top and bottom surfaces; the time history of the load is a step function. Experiments on specimens of similar dimensions have been reported by [24–28]. In these experiments, a crack starts growing at the notch and propagates to the right, generally with increasing speed. At a certain point, the crack branches into at least two cracks (some experiments show more branches). It is noteworthy that as shown in Fig. 13a, prior to the major branching, minor branches appear to start from the major crack but only grow to small lengths.

Figure 13b–d shows the evolution of the crack for a  $100 \times 41$  quadrilateral structured mesh at three different time steps as computed by XFEM. In these calculations, we used the Lemaitre damage law [29] for the continuum domain and



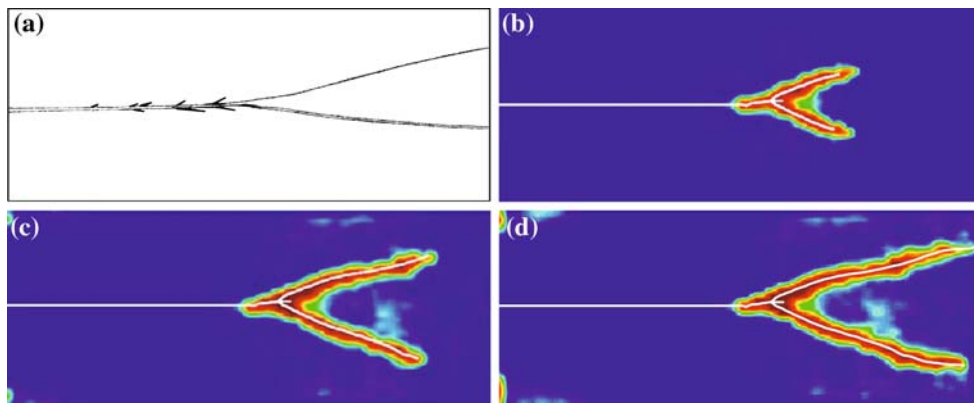
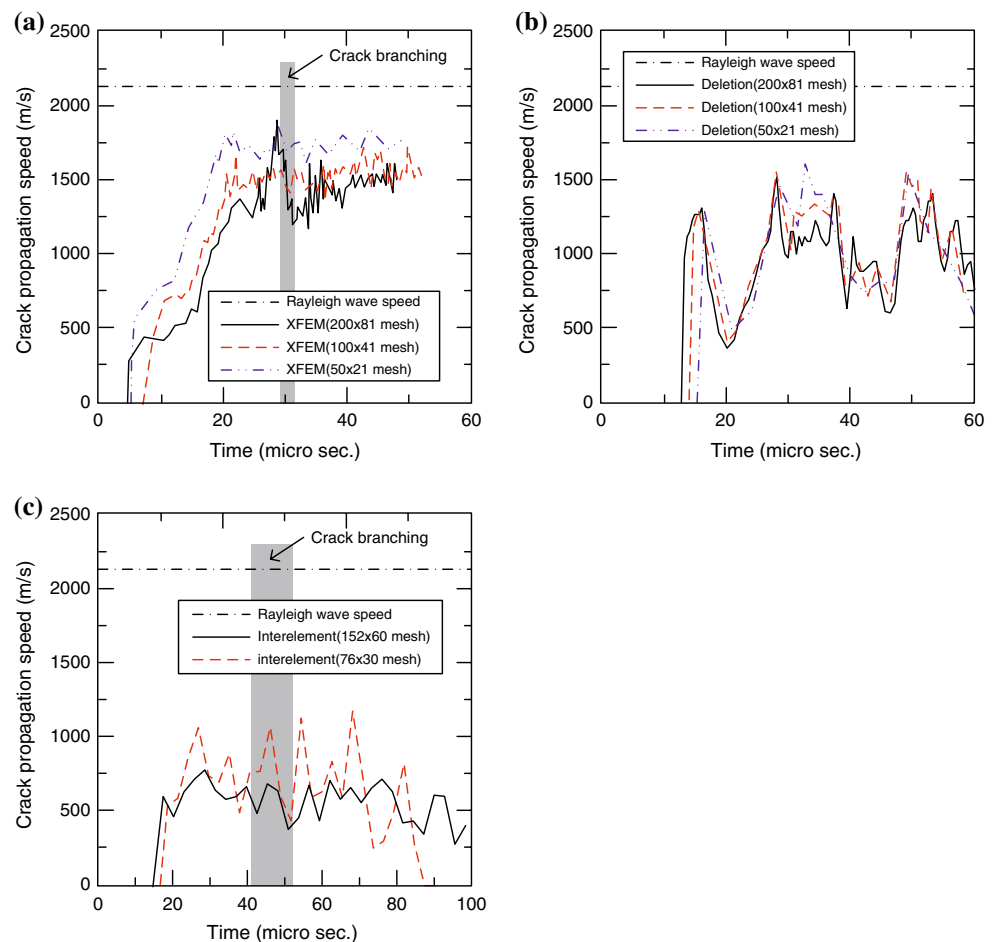


**Fig. 13** Comparison of the XFEM result with the experiment: **a** a sketch of the experiment crack paths reported by Ramulu and Kobayashi [24]; XFEM plots of crack branching and damage evolution with a  $100 \times 41$  quadrilateral mesh at **b**  $t = 39.29 \mu s$ , **c**  $t = 46.14 \mu s$  and **d**  $t = 55.93 \mu s$

**Fig. 14** Crack tip propagation speed for three different structured meshes: **a** the crack tip propagation speed of XFEM and **b** the crack tip propagation speed of the element deletion method (no crack branching occur), and **c** the crack tip propagation speed of interelement method [18]



imposed a linear cohesive law once a discontinuity developed by the material stability criterion. We used  $A = 1.0$ ,  $B = 7300.0$  and  $\epsilon_{D0} = 8.5 \times 10^{-5}$  for the Lemaitre damage model [29] and  $G_f = 3 \text{ Jm}^{-2}$  and  $\delta_{\max} = 1.95 \times 10^{-6} \text{ m}$  for the cohesive law. It can be seen that the major features of the crack path observed in the experiment are reproduced quite well. One phenomenon observed in the experiments

that is missing in the XFEM calculations is the tentative branches before the major branch emerges, but the general shape of the crack branching paths agree well with the experimental results. The results for  $200 \times 81$  and  $50 \times 21$  quadrilateral structured meshes are almost identical.

Figure 14a shows the crack tip velocity as computed by XFEM with three different structured quadrilateral meshes;

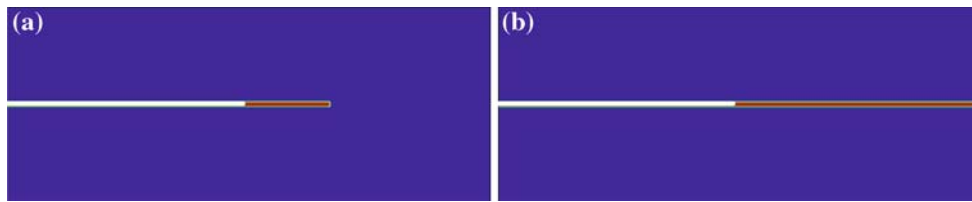


**Fig. 15** Final crack path of the element deletion method with a  $200 \times 81$  quadrilateral mesh at different time steps: **a**  $t = 30.56 \mu\text{s}$  and **b**  $t = 65.62 \mu\text{s}$

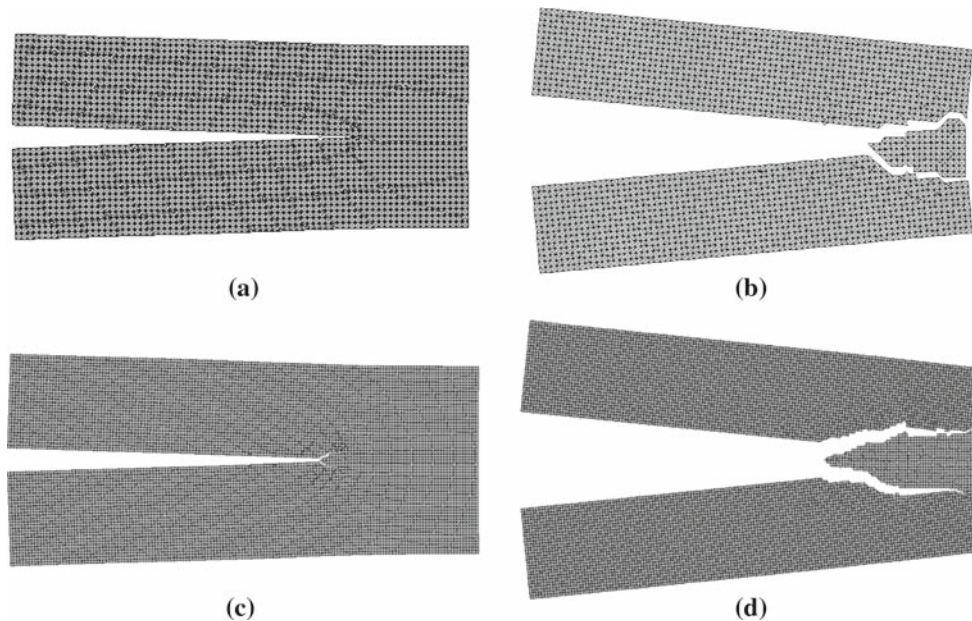


**Fig. 16** Crack path of the Camacho and Ortiz's method [18] with two structured cross-triangular meshes: the crack path of a  $76 \times 30$  structured cross-triangular mesh at **a**  $t = 48.38 \mu\text{s}$ ; **b**  $t = 100.00 \mu\text{s}$  and the crack

path of a  $152 \times 60$  structured cross-triangular mesh at **c**  $t = 48.09 \mu\text{s}$ ; **d**  $t = 100.0 \mu\text{s}$ . The deformed shapes are magnified by 90 times

i.e.  $h_e = 0.5, 1.0$  and  $2.0$  mm. As can be seen, once the crack starts growing, its velocity quickly increases to its maximum velocity of  $1,600$  m/s. As indicated in Fig. 14a, crack branching occurs  $30.0 \mu\text{s}$  after the maximum velocity is reached. The velocity shown after that point is the velocity of the top crack branch. The results show a substantial amount of mesh dependence in crack propagation speeds. Note that these results were obtained using an element-by-element progression of the crack; the XFEM method with partially cracked elements in Belytschko et al. [10] is less mesh dependent.

Figure 15 shows the results for the element deletion method at two different times. In these calculations, we used  $G_f = 3 \text{ Jm}^{-2}$  and  $\epsilon_0 = 8.50 \times 10^{-5}$  for Eqs. (7) and (8). It can be seen that the crack continues in a straight path without branching. The calculation shown was made with a  $200 \times 81$  mesh, but we have also used  $50 \times 21$  and  $100 \times 41$  meshes and obtained a straight crack with these meshes. One would expect the solution to exhibit an increase in the tensile strain

adjacent to the crack as its velocity increases, which would trigger crack branching. In the simulation by the element deletion method, the stress adjacent to the crack tip does increase, but it never becomes large enough to initiate crack propagation in the lateral direction. The crack tip speeds for three different meshes computed by the element deletion method are shown in Fig. 14b. It can be seen that the crack tip velocity for all meshes is significantly less than for XFEM. This is perhaps why branching does not occur. Also, the time history obtained by element deletion is completely different and bears little relationship to the results obtained by the other methods.

Figure 16a–d shows the crack paths obtained by the interelement crack method [18] for  $76 \times 30$  and  $152 \times 60$  structured cross-triangular meshes, respectively. In these calculations,  $\sigma_c = 2.8 \text{ MPa}$ ,  $\delta_c = 3.9 \times 10^{-7} \text{ m}$  and  $\beta = 1.0$  were used for Eq. (11). The crack tip speeds for  $76 \times 30$  and  $152 \times 60$  structured cross-triangular meshes computed by the interelement crack method are shown in Fig. 14c. The inter-



**Fig. 17** Final crack path for unstructured mesh ( $h_{avg}^e = 1.0$  mm): **a** the result of the element deletion and **b** the results of the Camacho and Ortiz's method [18]. The deformed shapes are magnified by 90 times

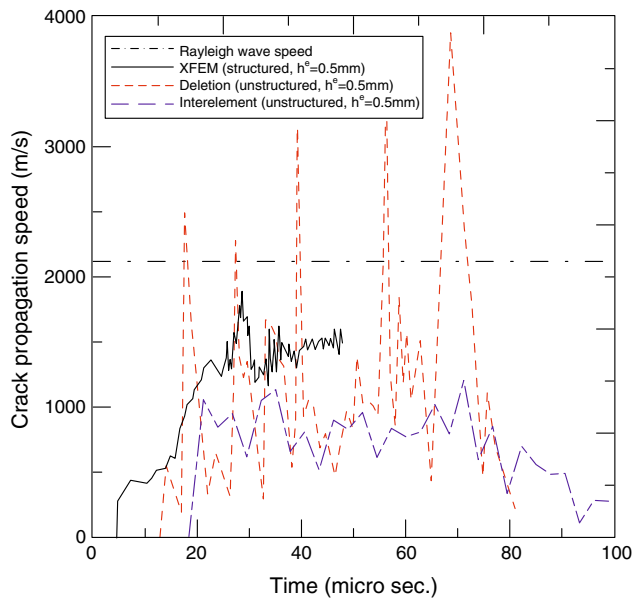
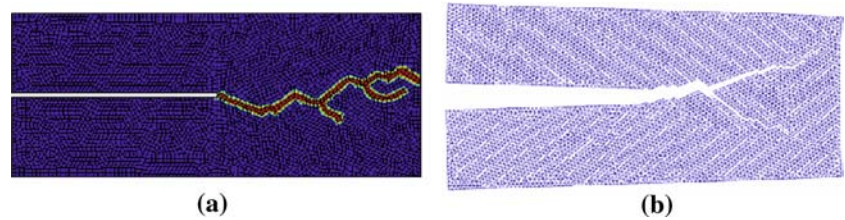


**Fig. 18** Comparison of the crack propagation speed for the crack branching problem

element method predicts crack branching but the branching point depends somewhat on mesh refinement.

Figure 17 shows the crack propagation paths and speeds for the interelement crack method along with the element deletion method for the unstructured mesh, respectively. As we can see from Fig. 17a, for an unstructured mesh the element deletion method predicts crack branching, but it is quite different from the experimental observation [24]. The crack speed of the interelement method is lower than that of XFEM and close to expected values; this reduction in speed again occurred due to parasitic cracks. The element deletion method for unstructured mesh gives a very irregular crack speed.

We should make some remarks about the crack nucleation criteria in the interelement method and in XFEM. In the interelement method, the crack propagation was modeled strictly by separation of element edges. The only aspect of the algorithm that limits the evolution of the crack is the transition from edges that share nodes (and thus can not separate) to edges that have duplicated nodes (and thus can separate). In XFEM, the crack growth was governed by the material stability criterion, which is a property of the constitutive equation used [in these computations, Eqs. (4) and (5)]. Crack

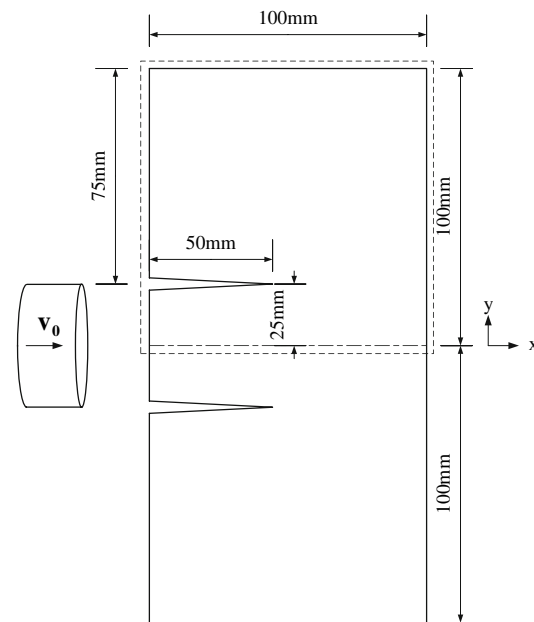


**Fig. 19** Experimental set up for edge-cracked plate under impulsive loading: dash line denotes the numerically modeled region

branching was initiated when the two polarization angles from the material stability analysis differed from that of the previous crack direction. When this occurred, the crack was also injected into the adjacent elements. Unless the latter step was taken, crack branching could not be modeled accurately with XFEM with low order elements.

### 5.3 Edge-cracked plate under impulsive loading

These simulations concern an experiment reported by Kalthoff and Winkler [30] in which a maraging steel 18Ni1900 plate with two initial edge notches is impacted by a projectile as shown in Fig. 19: the material properties [31] are  $\rho = 8,000$  kg/m<sup>3</sup>,  $E = 190$  GPa and  $\nu = 0.30$ . In the experiment, two different failure modes were observed by modifying the projectile speed,  $v_0$ ; at high impact velocities, a shear band is observed to emanate from the notch at an angle of  $-10^\circ$  with respect to initial notch; at lower strain rates, brittle failure with a crack propagation angle of about  $70^\circ$  is observed; see, Fig. 20a. We only studied the velocity range that resulted in a brittle fracture mode.

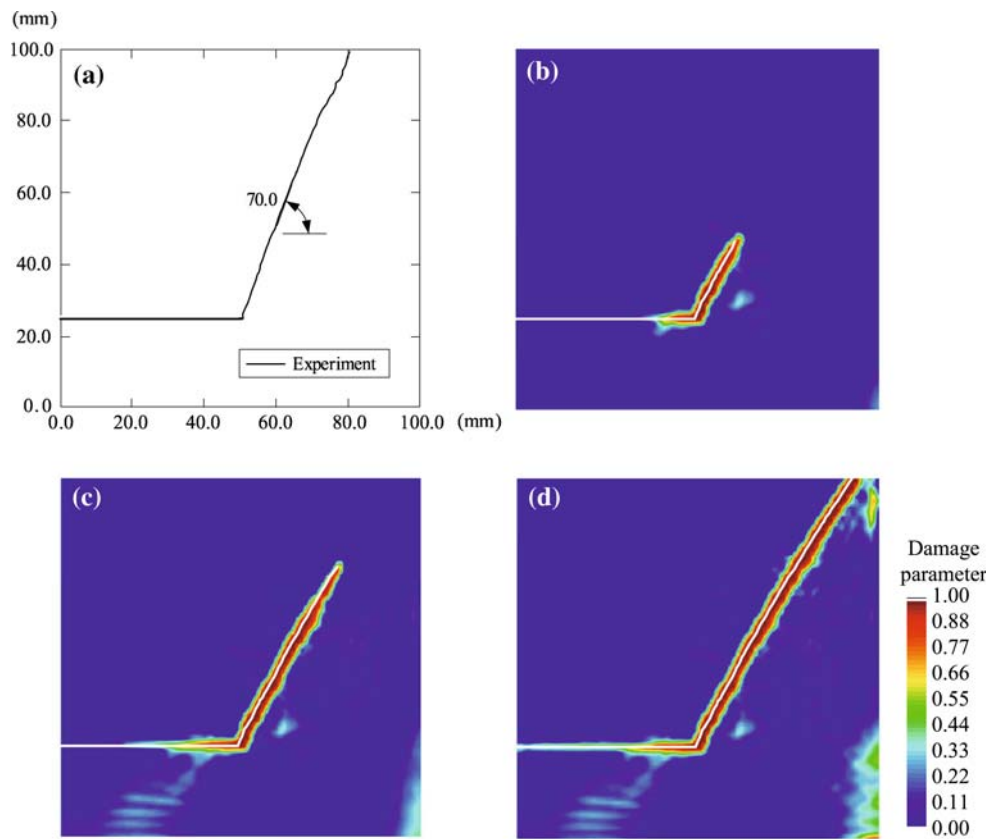


**Fig. 20** Comparison of the XFEM results with the experiment: **a** the experiment crack path reported by Kalthoff and Winkler [30]; XFEM crack path with a  $100 \times 100$  quadrilateral mesh at **b**  $t = 42.86 \mu\text{s}$ , **c**  $t = 53.58 \mu\text{s}$  and **d**  $t = 88.58 \mu\text{s}$

To take advantage of the twofold symmetry of the configuration, only the upper half of the plate is modelled: at the bottom edge of the finite element model,  $u_y = 0$  and  $t_x = 0$ . The initial impact velocity is applied on the left edge on the segment  $0 \leq y \leq 25 \text{ mm}$ . We assumed that the projectile has the same elastic impedance as the specimen, so we applied one half of the projectile speed,  $16.5 \text{ m/s}$  to the left edge as an initial condition (see, [32,33]).

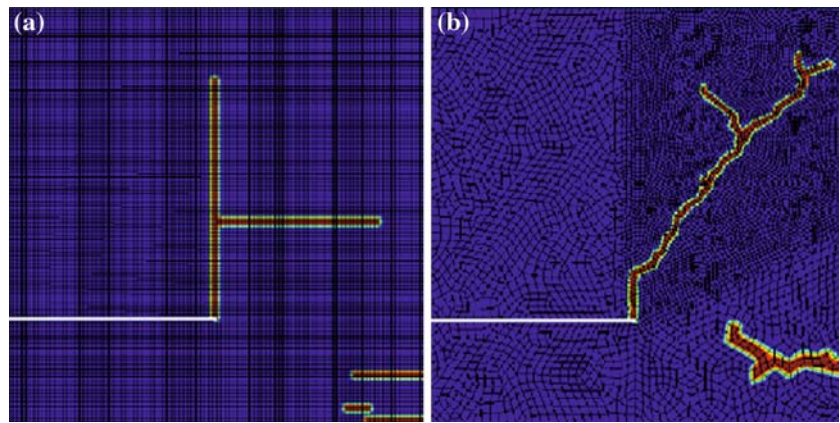
XFEM simulations were made with two different structured meshes:  $50 \times 50$  and  $100 \times 100$  meshes. In the calculations, we used  $A = 1.0$ ,  $B = 200.0$  and  $\varepsilon_{D_0} = 3.0 \times 10^{-3}$  for a Lemaitre damage constitutive model [29] and fracture energy  $G_f = 2.213 \times 10^4 \text{ N/m}$  and  $\delta_{\max} = 5.245 \times 10^{-5} \text{ m}$  for a linear cohesive law. The results for the  $100 \times 100$  mesh are shown in Fig. 20b–d. The simulation result with a  $50 \times 50$  mesh also shows very similar trajectories for the crack. The initial crack propagation angle is around  $64^\circ$  and the average angle from the initial crack tip to the final crack tip is about  $60^\circ$  for both meshes. This angle is  $10^\circ$  smaller than the experiment [30], but show little dependency on mesh size or mesh structure.

Figure 21a, b shows the crack paths computed by the element deletion method with a structured  $100 \times 100$  mesh

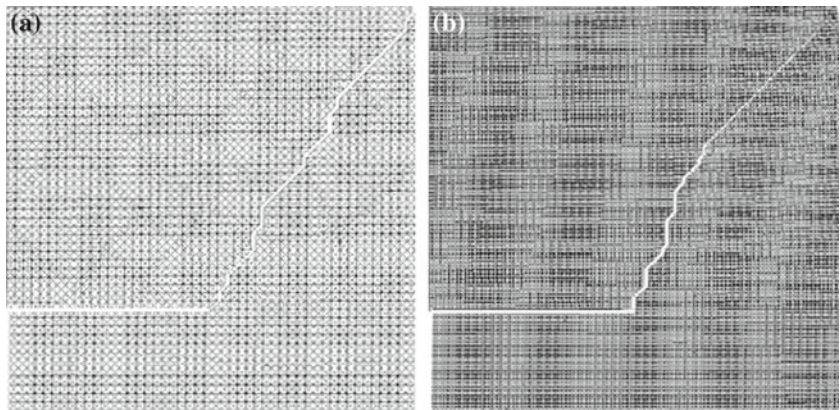
and equivalent unstructured mesh, respectively. In these calculations, we used  $G_f = 2.213 \times 10^4 \text{ N/m}$  and  $\epsilon_0 = 4.440 \times 10^{-3} \text{ m}$  for a linear elastic–elastic softening law in Eqs. (7) and (8). As we can see from Fig. 21a, a structured mesh cannot predict the experimental crack path and shows a severe pathological behavior. For an unstructured mesh, the crack first grows vertically upward and then grows at an angle of  $50^\circ$ . There are fractured areas in the bottom right corner of the model due to wave reflections.

Figure 22a, b shows the final crack path by the interelement crack method of the Xu and Needleman [17] with structured  $50 \times 50$  and  $100 \times 100$  meshes, respectively. In these calculations, we used  $\phi_n = \phi_t = 2.2170 \times 10^4 \text{ J/m}^2$ ,  $\delta_n = \delta_t = 4.720 \times 10^{-6} \text{ m}$ ,  $r = 0.0$  and  $q = 1.0$  for the Xu-Needleman's cohesive zone model [17]: see, Eq. (9). For a  $100 \times 100$  mesh, the crack initially propagates with an angle of  $70^\circ$ , which agrees quite well with the experiment, but after the mid point of the simulation, the crack suddenly propagates at a  $45^\circ$  angle. For the simulation with a  $50 \times 50$  mesh, there is no shift. The overall crack propagation angle is around  $55^\circ$ . For both meshes, crack paths meander along the  $90^\circ$  and  $45^\circ$  edges to achieve this angle.

**Fig. 21** Crack paths for the element deletion method with: **a**  $100 \times 100$  quadrilateral mesh at  $t = 60.19 \mu\text{s}$  and **b** unstructured mesh  $h_{\text{avg}}^e = 1.0 \text{ mm}$ , at  $t = 67.85 \mu\text{s}$



**Fig. 22** The final crack path of the interelement crack method of the Xu–Needleman method [17] with  $50 \times 50$  and  $100 \times 100$  quadrilateral meshes: **a**  $t = 98.65 \mu\text{s}$  and **b**  $t = 98.73 \mu\text{s}$



## 6 Conclusions

Three benchmark problems in dynamics crack propagation have been studied by

1. the extended finite element method
2. the interelement crack method
3. the element deletion method.

None of these methods are currently able to accurately predict crack propagation velocities and paths for all of the relatively simple problems that were tackled here.

In the first benchmark problem, the major difficulty encountered is the dependence of crack speed on subscale phenomena; these are discussed in [23,27,34]. The interelement method and XFEM performed reasonably well when the fracture energy was tuned to the experimental results, but without such tuning, the computed crack speeds were substantially too high. One could of course improve the predictions by developing velocity-dependent fracture energies, but it is not clear how universal such laws would be. The element deletion method substantially underpredicted the crack speed, and we have not been able to explain this, because for a straight crack the method should behave like the interelement method or XFEM.

The element deletion method performed especially poorly for crack paths that are not coincident with meshlines. It is somewhat perplexing that this method is widely used in industry and has performed reasonably in predicting the gross features of certain experiments. Bourdin et al. [35] have shown large scale calculations that model curved cracks very accurately; this method is essentially of the element deletion genre with regularization. So, perhaps in the context of million element simulations, the element deletion method will improve.

A major shortcoming of XFEM is the need to inject the discontinuity on the basis of a failure criterion, and that its use of level sets tends to favor the propagation of a single crack. Methods that can inject a crack arbitrarily, such as proposed by Remmers et al. [16], may be more suitable for arbitrary crack propagation. Rabczuk and Belytschko [36] have already solved some complex problems of crack propagation and fragmentation by this approach in a meshless method, but the results are not as accurate as those of XFEM.

The interelement method appears to be more adaptable to simulating crack nucleation than XFEM. However, the crack paths predicted by the interelement method tend to be somewhat inaccurate. This could be remedied by much finer meshes or perhaps by special meshing schemes, such as that of Papoulia et al. [37].



Nevertheless, it is clear that the problem of computationally predicting brittle dynamic fracture with a high degree of accuracy is not closed. Aside from the issues of suitable failure criteria for various materials, difficulties remain in modeling complex crack paths, such as those involving branching and in achieving mesh independence. Furthermore, accurate predictive methods may require multiscale approaches that model subscale phenomena, such as those that occur after critical crack speeds. The prediction of crack paths for more complex scenarios which were not considered here, such as fragmentation, also is an open problem.

**Acknowledgments** The support of the Office of Naval Research under Grant N00014-06-1-0380 and N00014-03-1-0097 are gratefully acknowledged.

## References

1. Ravi-Chandar K, Knauss WG (1984) An experimental investigation into dynamic fracture: II. microstructural aspects. *Int J Fract* 26:65–80
2. Ravi-Chandar K, Knauss WG (1984) An experimental investigation into dynamic fracture: III. on steady-state crack propagation and crack branching. *Int J Fract* 26:141–154
3. Ravi-Chandar K (2004) *Dynamic fracture*. Elsevier, Boston
4. Marder M, Gross S (1995) Origin of crack tip instabilities. *J Mech Phys Solids* 43(1):1–48
5. Belytschko T, Black T (1999) Elastic crack growth in finite elements with minimal remeshing. *Int J Numer Meth Eng* 45(5):601–620
6. Moës N, Dolbow J, Belytschko T (1999) A finite element method for crack growth without remeshing. *Int J Numer Meth Eng* 46(1):131–150
7. Stolarska M, Chopp DL, Moës N, Belytschko T (2001) Modeling crack growth by level sets in the extended finite element method. *Int J Numer Meth Eng* 51(8):943–960
8. Belytschko T, Moës N, Usui S, Parimi C (2001) Arbitrary discontinuities in finite elements. *Int J Numer Meth Eng* 50(4):993–1013
9. Babuška I, Melenk JM (1997) The partition of unity method. *Int J Numer Meth Eng* 40(4):727–758
10. Belytschko T, Chen H, Xu J, Zi G (2003) Dynamic crack propagation based on loss of hyperbolicity with a new discontinuous enrichment. *Int J Numer Meth Eng* 58:1873–1905
11. Song J-H, Areias PMA, Belytschko T (2006) A method for dynamic crack and shear band propagation with phantom nodes. *Int J Numer Meth Eng* 67:868–893
12. Hansbo A, Hansbo P (2004) A finite element method for the simulation of strong and weak discontinuities in solid mechanics. *Comput Meth Appl Mech Eng* 193:3523–3540
13. Areias PMA, Belytschko T (2006) A comment on the article: a finite element method for simulation of strong and weak discontinuities in solid mechanics. *Comput Meth Appl Mech Eng* 195:1275–1276
14. Réthoré J, Gravouil A, Combescure A (2004) A stable numerical scheme for the finite element simulation of dynamic crack propagation with remeshing. *Comput Meth Appl Mech Eng* 193:42–44
15. Réthoré J, Gravouil A, Combescure A (2005) An energy-conserving scheme for dynamic crack growth using the extended finite element method. *Int J Numer Meth Eng* 63:631–659
16. Remmers JJC, Borst R, de Needleman A (2003) A cohesive segments method for the simulation of crack growth. *Comput Mech* 31:69–77
17. Xu X-P, Needleman A (1994) Numerical simulation of fast crack growth in brittle solids. *J Mech Phys Solids* 42(9):1397–1434
18. Camacho G, Ortiz M (1996) Computational modelling of impact damage in brittle materials. *Int J Solids Struct* 33:2899–2938
19. Lemaitre J, Chaboche JL (1990) *Mechanics of solid materials*. Cambridge University Press, Cambridge. ISBN 0 521 32853 5
20. Hallquist JO (1998) *LS-DYNA theory manual*. Livemore software technology corporation, USA
21. Ortiz M, Pandolfi A (1999) A class of cohesive elements for the simulation of three-dimensional crack propagation. *Int J Numer Meth Eng* 44:1267–1282
22. Fineberg J, Gross SP, Marder M, Swinney HL (1991) Instability in dynamic fracture. *Phys Rev Lett* 67:457–460
23. Sharon E, Fineberg J (1999) Confirming the continuum theory of dynamic brittle fracture for fast cracks. *Lett Nature* 397:333–335
24. Ramulu M, Kobayashi AS (1985) Mechanics of crack curving and branching—a dynamic fracture analysis. *Int J Fract* 27:187–201
25. Ravi-Chandar K (1998) Dynamic fracture of nominally brittle materials. *Int J Fract* 90:83–102
26. Sharon E, Gross SP, Fineberg J (1995) Local crack branching as a mechanism for instability in dynamic fracture. *Phys Rev Lett* 74(25):5096–5099
27. Sharon E, Fineberg J (1996) Microbranching instability and the dynamic fracture of brittle materials. *Phys Rev B* 54(10):7128–7139
28. Fineberg J, Sharon E, Cohen G (2003) Crack front waves in dynamic fracture. *Int J Fract* 119:247–261
29. Lemaitre J (1971) Evaluation of dissipation and damage in metal submitted to dynamic loading. In: *Proceedings ICM 1*
30. Kalthoff JF, Winkler S (1987) Failure mode transition at high rates of shear loading. *International conference on impact loading and dynamic behavior of materials*, vol 1. pp 185–195
31. Decker RF (1979) *Source book on maraging steels*. American Society for Metals
32. Lee YJ, Freund LB (1990) Fracture initiation due to asymmetric impact loading of an edge cracked plate. *J Appl Mech ASME* 57:104–111
33. Kalthoff JF (2000) Modes of dynamic shear failure in solids. *Int J Fract* 101:1–31
34. Sharon E, Gross SP, Fineberg J (1996) Energy dissipation in dynamic fracture. *Phys Rev Lett* 76(12):2117–2120
35. Bourdin B, Francfort GA, Marigo JJ (2000) Numerical experiments in revisited brittle fracture. *J Mech Phys Solids* 48(4):797–826
36. Rabczuk T, Belytschko T (2004) Cracking particles: a simplified meshfree method for arbitrary evolving cracks. *Int J Numer Meth Eng* 61(13):2316–2343
37. Papoulia KD, Vavasis SA, Ganguly P (2006) Spatial convergence of crack nucleation using a cohesive finite-element model on a pinwheel-based mesh. *Int J Numer Meth Eng* 67:1–16